# BUCKLING OPTIMIZATION AND PREBUCKLING ENHANCEMENT OF IMPERFECT COMPOSITE PLATES USING PIEZOELECTRIC ACTUATORS

**Alfredo R. de Faria**[a]

[a]*Department of Mechanical Engineering, Instituto Tecnológico de Aeronáutica, CTA - ITA - IEM, São José dos Campos, SP 12228-900, Brazil, arfaria@ita.br, http://www.mec.ita.br/~arfaria*

**Keywords:** Prebuckling, piezoelectric effect, initial imperfections, composites.

**Abstract.** An imperfect composite plate equipped with piezoelectric actuators is investigated. Geometric nonlinear effects are considered only in the prebuckling regime such that higher order strain energy terms can be disregarded. The actuators are used to achieve two goals: to optimize buckling loads under uncertain loadings via stress stiffening effects and to ameliorate the plate prebuckling response through application of piezoelectric bending moments. A strategy is proposed where the piezoelectric membrane forces and bending moments are separated by proper selection of voltages imposed on symmetrically bonded piezoelectric patches. Piezoelectric forces and moments are then used separately to optimize buckling loads and to improve prebuckling response.

## 1 INTRODUCTION

Smart or intelligent structures can be very useful when it comes to the design of systems with superior performance. Their advantage over passive structures resides in the fact that they can adapt or adjust in response to the applied loadings in order to perform according to stringent design requirements. Active materials are essential for the struture to adapt. Sensors monitor the structure behavior and actuators apply corrective forces, displacements or deformations. A control system is usually in charge of processing the input data collected by the sensors and feeding the result back to the actuators.

Piezoelectric materials were much in evidence especially in the '80s (Crawley and de Luis, 1987) and '90s (Reddy, 1997) when a large number of applications could be envisioned, from damping to active noise suppression, through sophisticated applications such as the morphing wing. Its relatively low cost, small size and good characteristic frequency response indicated that piezoelectric materials would be an attractive alternative over traditional actuators. However, much of what was preached in relation to piezoelectric materials has proved of limited applicability. Today there is a return of piezoelectric materials to scientific and technological scenario, but within a more realistic context.

On the other hand, the processing power of computers has increased considerably since the '90s, allowing the analysis of complex structures of composite materials using the finite element method (FEM). In addition, there was an improvement in algorithms specifically designed for solving static and dynamic, linear and nonlinear problems, opening up some new possibilities for research which consider piezoelectric and highly nonlinear effects together. Among these new possibilities, there is, for instance, the numerical simulation (using FEM) of composite structures subjected to large displacements and small deformations, where the linear regime of the material remains valid and the nonlinearities are limited to those of geometric nature.

In a time were costs and environment impact must be reduced the use of lightweight composite structures is becoming indispensable. Minimization of mass, however, implies in reduced stiffness or higher flexibility what leads to larger displacements and rotations and evetually to nonlinear behavior. Hence, accurate modes to predict nonlinear response of composite structures are increasingly necessary. A coupled buckling and postbuckling analysis of composite plate with piezoelectric actuators was presented by Varelis and Saravanos (2004). Their work addresses the nonlinear response of smart plates when acted upon by piezoelectric membrane forces and bending moments, whose nonlinear governing equations are numerically solved. A correlated work by Rabinovitch (2005) investigates the geometrical nonlinear response of composite smart plates. Initial imperfections in both papers just cited are only included through application of small disturbance forces to perturb the equilibrium path of otherwise perfect structures. Moreover, stress stiffening effects are not treated at all.

Buckling enhancement of structures equipped with piezoelectric patches has been profusely investigated (Chandrashenkhara and Bathia, 1993; Meressi and Paden, 1993) For example, Correia et al. (2005) used simulated annealing to obtain the optimal location of actuators and optimal fiber orientations to maximize buckling loads of smart composite plates. Their work is however limited to the linear regime and only linearized optimal buckling loads are evaluated.

The proposal of this paper is to employ piezoelectric actuators to control or correct the equilibrium path of imperfect composite plates. The piezoelectric effect is used in two ways: (i) the piezoelectric stress stiffening effect maximizes the buckling load in the presence of uncertain loadings, and (ii) the piezoelectric bending moment actuation corrects the equilibrium path. It is shown that mechanisms (i) and (ii) are entwined, i.e., the higher the buckling load, the easier

it is for the control to correct the equilibrium path. Therefore, the importance of maximizing the buckling load is utmost. The strategy proposed is implemented by splitting the voltages ($\phi$) applied to the active patches into two components: $\phi_N$ and $\phi_M$, $\phi_N$ produces membrane forces whereas $\phi_M$ produces bending moments. Is is shown that the proposed technique simultaneously increases buckling loads and ameliorates initial imperfection effects.

557

## 2 PROBLEM FORMULATION

The composite smart plate considered contains patches of piezoelectric actuators symmetrically bonded to its top and bottom surfaces. The mathematical foundation describing the electromechanical behavior of the laminated plate is based on Mindlin plate theory since the thickness is assumed small. A perfect the piezoelectric patches are assumed to be perfect capacitors with constant electric field in the transverse direction, leading to voltages that vary linearly through the thickness of these patches.

A rectangular composite plate with one pair of piezoelectric patches attached is depicted in Fig. 1. The bottom patch is not shown.

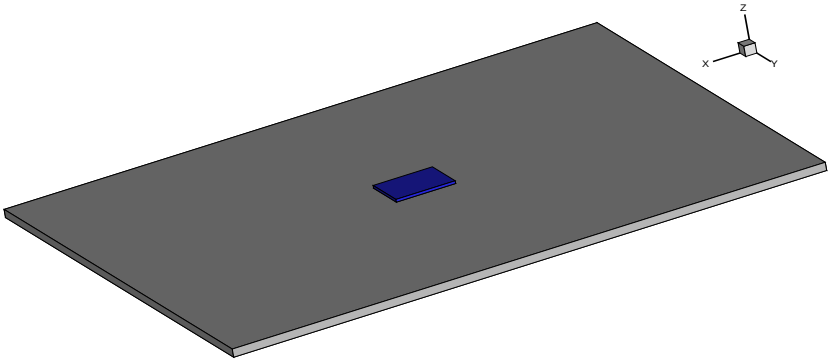


Figure 1: Basic configuration

Equation (1) gives the constitutive equations, assuming polarization along the $z$ direction (perpendicular to the plate).

$$\overline{\boldsymbol{\sigma}} = \mathbf{C}\overline{\boldsymbol{\epsilon}} - \mathbf{e}^T\mathbf{E}, \quad \mathbf{d} = \mathbf{e}\overline{\boldsymbol{\epsilon}} + \boldsymbol{\xi}\mathbf{E}, \tag{1}$$

where $\overline{\boldsymbol{\sigma}}$ is a vector of stresses, $\mathbf{C}$ is the ply stiffness matrix, $\overline{\boldsymbol{\epsilon}}$ are the strains including linear, nonlinear and imperfection components, $\mathbf{e}$ is the electro-mechanical coupling matrix, $\mathbf{E}$ is the electric field, $\mathbf{d}$ is the electric displacement, and $\boldsymbol{\xi}$ is the permitivitty matrix. All matrices and vectors in Eq. (1) related to the *structural* coordinate system. Thus, the proper coordinate transformations of principal to strcutural coordinate systems have already been made. Equation (1) applies to both composite and piezoelectric materials. When the electro-mechanical coupling is not present, i.e., in a purely composite layer, matrices $\mathbf{e}$ and $\boldsymbol{\xi}$ are zeroed.

The system total potential energy is given by:

$$\Pi = \frac{1}{2}\int_V \overline{\boldsymbol{\sigma}}^T\overline{\boldsymbol{\epsilon}}dV - \frac{1}{2}\int_V \mathbf{d}^T\mathbf{E}dV - W, \tag{2}$$

where $V$ is the entire domain including composite and piezoelectric materials, and $W$ is the work of external forces $N_{xx0}$, $N_{yy0}$, $N_{xy0}$. The in-plane strain vector $\boldsymbol{\epsilon}$ can be split into four components as given in Eq. (3): membrane strains $\boldsymbol{\epsilon}_0$, curvature $\boldsymbol{\kappa}$, nonlinear von Karman

strains $\boldsymbol{\epsilon}_N$ and geometric imperfections $\boldsymbol{\epsilon}^*$. The transverse shear strains $\boldsymbol{\gamma}$ are not affected by electro-mechanical effects and do not possess nonlinear components if moderate rotations are considered.

$$\boldsymbol{\epsilon} = \boldsymbol{\epsilon}_0 + z\boldsymbol{\kappa} + \boldsymbol{\epsilon}_N + \boldsymbol{\epsilon}^*,$$

$$\boldsymbol{\epsilon}_0 = \left\{ \begin{array}{c} u_{,x} \\ v_{,y} \\ u_{,y} + v_{,x} \end{array} \right\}, \quad \boldsymbol{\kappa} = \left\{ \begin{array}{c} \psi_{x,x} \\ \psi_{y,y} \\ \psi_{x,y} + \psi_{y,x} \end{array} \right\}, \quad \boldsymbol{\epsilon}_N = \frac{1}{2} \left\{ \begin{array}{c} w_{,x}^2 \\ w_{,y}^2 \\ 2w_{,x}w_{,y} \end{array} \right\},$$

$$\boldsymbol{\epsilon}^* = \left\{ \begin{array}{c} w_{,x}w_{,x}^* \\ w_{,y}w_{,y}^* \\ w_{,x}w_{,y}^* + w_{,y}w_{,x}^* \end{array} \right\}, \quad \boldsymbol{\gamma} = \left\{ \begin{array}{c} w_{,x} + \psi_x \\ w_{,y} + \psi_y \end{array} \right\}, \tag{3}$$

where $\psi_x$ and $\psi_y$ are the traditional rotations included in Mindlin theory. Elastic displacements at point (x,y,z) are given by $\tilde{u}(x,y,z) = u(x,y) + z\psi_x(x,y)$, $\tilde{v}(x,y,z) = v(x,y) + z\psi_y(x,y)$ and $\tilde{w}(x,y,z) = w(x,y)$. Hence, within the scope of Mindlin theory, Eq. (1) reduces to

$$\boldsymbol{\sigma} = \overline{\mathbf{Q}}\boldsymbol{\epsilon} - \mathbf{e}'E_z, \quad \boldsymbol{\tau} = \overline{\mathbf{Q}}_S\boldsymbol{\gamma}, \quad d_z = (\mathbf{e}')^T\boldsymbol{\epsilon} + \xi_{zz}E_z, \tag{4}$$

where $\boldsymbol{\sigma} = \{ \begin{array}{ccc} \sigma_{xx} & \sigma_{yy} & \tau_{xy} \end{array} \}^T$, $\overline{\mathbf{Q}}$ is the in-plane ply stiffness matrix in the structural coordinate system, $\boldsymbol{\epsilon} = \{ \begin{array}{ccc} \epsilon_{xx} & \epsilon_{yy} & \gamma_{xy} \end{array} \}^T$, $\mathbf{e}' = \{ \begin{array}{ccc} e_{31} & e_{31} & 0 \end{array} \}^T$, $E_z$ is the electric field perpendicular to the plate, $\boldsymbol{\tau} = \{ \begin{array}{cc} \tau_{xz} & \tau_{yz} \end{array} \}^T$, $\overline{\mathbf{Q}}_S$ is the transverse ply stiffness matrix in the structural coordinate system, $\boldsymbol{\gamma} = \{ \begin{array}{cc} \gamma_{xz} & \gamma_{yz} \end{array} \}^T$, and $d_z$ is the electric displacement. Transformation of the coordinate system yields $\mathbf{e}'$ provided it is assumed that $e_{31} = e_{32}$, what is valid for transversely isotropic piezoelectric materials Nye, 1972).

Manipulation of Eq. (2) is facilitated if matrices **A**, **B**, **D**, and $\mathbf{A}_S$ and vectors $\mathbf{N}_p$, $\mathbf{M}_p$ are defined as

$$\begin{aligned} (\mathbf{A}, \mathbf{B}, \mathbf{D}) &= \int_{-h/2}^{h/2} (1, z, z^2)\overline{\mathbf{Q}}dz \\ \mathbf{A}_S &= \int_{-h/2}^{h/2} \overline{\mathbf{Q}}_S dz \\ (\mathbf{N}_p, \mathbf{M}_p) &= \int_{-h/2}^{h/2} (1, z)\mathbf{e}'E_z dz, \end{aligned} \tag{5}$$

where $h$ is the total laminate thickness. Notice that the piezoelectric patches contribute to the stiffness matrices **A**, **B**, **D** and $\mathbf{A}_S$. Also, vectors $\mathbf{N}_p$, and $\mathbf{M}_p$ are nonzero only if there are piezoelectric layers present in the laminate.

Consistent with the perfect capacitor assumption, $E_z = \phi/t$, where $\phi$ is voltage and $t$ is thickness. When there are two piezoelectric patches, one each attached to the top ($T$) and one to the bottom ($B$) of the plate surfaces, the electric fields $E_z$ are $\phi_T/t_T$ and $\phi_B/t_B$. In practice $t_T = t_B = t$ which allows $\phi_T$ and $\phi_B$ to be written as $\phi_T = \phi_N + \phi_M$ and $\phi_B = \phi_N - \phi_M$, respectively. In this situation Eq. (5c) simplifies to

$$\mathbf{N}_p = 2\mathbf{e}'\phi_N, \qquad \mathbf{M}_p = \mathbf{e}'(h-t)\phi_M. \tag{6}$$

Introducing Eqs. (3) and (4) into (2) yields

$$\Pi = \frac{1}{2}\int_V (\boldsymbol{\epsilon}_0+z\boldsymbol{\kappa})^T\overline{\mathbf{Q}}(\boldsymbol{\epsilon}_0+z\boldsymbol{\kappa})dV+\frac{1}{2}\int_V \boldsymbol{\gamma}^T\overline{\mathbf{Q}}_S\boldsymbol{\gamma}dV+\int_V(\boldsymbol{\epsilon}_N+\boldsymbol{\epsilon}^*)^T[\overline{\mathbf{Q}}(\boldsymbol{\epsilon}_0+z\boldsymbol{\kappa})-\mathbf{e}'E_z]dV-$$

$$\int_V(\boldsymbol{\epsilon}_0+z\boldsymbol{\kappa})^T\mathbf{e}'E_z dV-\frac{1}{2}\int_V \xi_{zz}E_z^2 dV+\frac{1}{2}\int_V(\boldsymbol{\epsilon}_N+\boldsymbol{\epsilon}^*)^T\overline{\mathbf{Q}}(\boldsymbol{\epsilon}_N+\boldsymbol{\epsilon}^*)dV-W. \tag{7}$$

The last integral can be neglected in the prebuckling regime. Thus, Eq. (7) can be modified by using Eqs. (5) and (6) and computation of the work term $W$ to

$$\Pi = \frac{1}{2}\int_\Omega \left\{\begin{array}{c}\boldsymbol{\epsilon}_0\\ \boldsymbol{\kappa}\end{array}\right\}^T\left[\begin{array}{cc}\mathbf{A}&\mathbf{B}\\ \mathbf{B}&\mathbf{D}\end{array}\right]\left\{\begin{array}{c}\boldsymbol{\epsilon}_0\\ \boldsymbol{\kappa}\end{array}\right\}d\Omega+\frac{1}{2}\int_\Omega\boldsymbol{\gamma}^T\mathbf{A}_S\boldsymbol{\gamma}d\Omega+$$

$$\int_\Omega(\boldsymbol{\epsilon}_N+\boldsymbol{\epsilon}^*)^T(\mathbf{A}\boldsymbol{\epsilon}_0+\mathbf{B}\boldsymbol{\kappa}-\mathbf{N}_p)d\Omega-\int_\Omega\boldsymbol{\epsilon}_0^T\mathbf{N}_p d\Omega-\int_\Omega\boldsymbol{\kappa}^T\mathbf{M}_p d\Omega-$$

$$\int_\Omega\frac{\xi_{zz}}{t}(\phi_N^2+\phi_M^2)d\Omega-\int_\Gamma(N_{xx0},N_{xy0})\cdot\vec{n}\,u d\Gamma-\int_\Gamma(N_{xy0},N_{yy0})\cdot\vec{n}\,v d\Gamma. \tag{8}$$

where $\Omega$ is the plane $xy$ domain of the plate and $\vec{n}$ is the unit vector normal to $\Gamma$, the boundary of $\Omega$. In practical configuration the laminate is symmetric resulting in $\mathbf{B}=\mathbf{0}$. Moreover, if olny actuation is admitted, $\phi_N$ and $\phi_M$ are prescribed, such that the integral reflecting electric energy (fifth integral in Eq. (7)) is not subject to variation and can be eliminated. Therefore,

$$\Pi = \frac{1}{2}\int_\Omega\boldsymbol{\epsilon}_0^T\mathbf{A}\boldsymbol{\epsilon}_0 d\Omega+\frac{1}{2}\int_\Omega\boldsymbol{\kappa}^T\mathbf{D}\boldsymbol{\kappa}d\Omega+\frac{1}{2}\int_\Omega\boldsymbol{\gamma}^T\mathbf{A}_S\boldsymbol{\gamma}d\Omega+$$

$$\int_\Omega(\boldsymbol{\epsilon}_N+\boldsymbol{\epsilon}^*)^T(\mathbf{A}\boldsymbol{\epsilon}_0-\mathbf{N}_p)d\Omega-\int_\Omega\boldsymbol{\epsilon}_0^T\mathbf{N}_p d\Omega-\int_\Omega\boldsymbol{\kappa}^T\mathbf{M}_p d\Omega-$$

$$\int_\Gamma(N_{xx0},N_{xy0})\cdot\vec{n}\,u d\Gamma-\int_\Gamma(N_{xy0},N_{yy0})\cdot\vec{n}\,v d\Gamma. \tag{9}$$

Observe that, according to Eq. (6), $\mathbf{N}_p$ and $\mathbf{M}_p$ depend only on $\phi_N$ and $\phi_M$, respectively. Thus, $\phi_N$ related solely to piezoelectric membrane forces whereas $\phi_M$ related solely to piezoelectric bending moments. The dependance of $\mathbf{N}_p$ and $\mathbf{M}_p$ with the voltages applied to the top and bottom piezoelectric is now clearly established.

Making the first variation of $\Pi$ equal to zero results in the governing equilibrium equations which are only weakly coupled in the displacement degrees of freedom. Notice that $\boldsymbol{\epsilon}_0$ is the only strain component that depends on displacements $u$, $v$. $\boldsymbol{\kappa}$, $\boldsymbol{\epsilon}^N$ and $\boldsymbol{\epsilon}^*$ depend on $w$, $\psi_x$, $\psi_y$. Closer observation of Eq. (9) shows that the fourth integral involves both $\boldsymbol{\epsilon}_0$ and $\boldsymbol{\epsilon}^N$. The fourth integral describes precisely the stress stiffening effects. Stiffening effects may result from two sources: (i) the conventional mechanical stresses $\mathbf{N}_0$ related to the application of external forces $N_{xx0}$, $N_{yy0}$, $N_{xy0}$, and (ii) piezoelectric residual stresses due to $\mathbf{N}_p^R=\mathbf{A}\boldsymbol{\epsilon}_0-\mathbf{N}_p$. However, the residual stresses $\mathbf{N}_p^R$ are nonzero only when the plate is constrained from moving in the $xy$ plane, what is often a configuration of practical relevance in real structures attached to primary structural components or to the ground. One objective of this work is to use piezoelectric stress stiffening to increase structural stiffness thereby increasing buckling loads. For that purpose, term $(\mathbf{A}\boldsymbol{\epsilon}_0-\mathbf{N}_p)$ must be nonzero and must be retained in the bending equation. Nevertheless, it is neglected in the membrane equation since it carries fundamentaly terms that are of third order in the displacements and their derivatives with respect to $x$ and $y$.

The structural problem $\delta\Pi = 0$ may now be split into two uncoupled problems:

$$\Pi_N = \frac{1}{2}\int_\Omega \boldsymbol{\epsilon}_0^T \mathbf{A}\boldsymbol{\epsilon}_0 d\Omega - \int_\Omega \boldsymbol{\epsilon}_0^T \mathbf{N}_p d\Omega - \int_\Gamma (N_{xx0}, N_{xy0})\cdot\vec{n}\, u d\Gamma - \int_\Gamma (N_{xy0}, N_{yy0})\cdot\vec{n}\, v d\Gamma,$$

$$\Pi_M = \frac{1}{2}\int_\Omega \boldsymbol{\kappa}^T \mathbf{D}\boldsymbol{\kappa} d\Omega + \frac{1}{2}\int_\Omega \boldsymbol{\gamma}^T \mathbf{A}_S\boldsymbol{\gamma} d\Omega + \int_\Omega (\boldsymbol{\epsilon}_N + \boldsymbol{\epsilon}^*)^T(\mathbf{N}_0 + \mathbf{N}_p^R) d\Omega - \int_\Omega \boldsymbol{\kappa}^T \mathbf{M}_p d\Omega. \quad (10)$$

The membrane problem $\delta\Pi_N = 0$ is solved after specification of $\phi_N$, $N_{xx0}$, $N_{yy0}$ and $N_{xy0}$. Its solution gives the piezoelectric residual stresses $\mathbf{N}_p^R$. Numerically the membrane problem is solved in two steps: (i) voltages $\phi_N$ are applied and $\mathbf{N}_p^R$ is computed and (ii) external forces $N_{xx0}$, $N_{yy0}$, $N_{xy0}$ are applied and mechanical stresses $\mathbf{N}_0$ are computed. Once $\mathbf{N}_p^R$ and $\mathbf{N}_0$ are computed the bending problem $\delta\Pi_M = 0$ can be solved admitting that voltages $\phi_M$ are known.

## 3 FINITE ELEMENT FORMULATION

Unfortunately, Eq. (10) does not admit closed form solution. Even when traditional uniformly distributed loadings $N_{xx0}$, $N_{yy0}$, $N_{xy0}$ are applied the piezoelectric pacthes locally change the plate stiffness what obliterates the possibility of analytical solution to the membrane problem. Therefore, the problems $\delta\Pi_N = 0$ and $\delta\Pi_M = 0$ must be numerically solved.

A finite element code was specially written to solve for the smart composite plate under investigation. It employs biquadratic Lagrange elements to interpolate five degrees of freedom: $u$, $v$, $w$, $\psi_x$ and $\psi_y$. Interpolation of the voltages is unnecessary because $\phi$ is constant within an element. $w^*(x, y)$ are known geometric imperfections unaffected by the variational operator ($\delta$).

Real structures are subjected to several mechanical load cases which, in a preliminary stage, may be approximated by linear combinations of conventional uniform distrubuted loadings corresponding to normal compression in the $x$ and $y$ directions and shear. The linear combinations are determined by assigning load ratios $R_i$ to each admissible mechanical loading. In the smart composite plate considered three load ratios exist: $R_{xx}$ for mechanical load $N_{xx0}$, $R_{yy}$ for mechanical load $N_y$, and $R_{xy}$ for mechanical load $N_{xy0}$. This particular description of loadings is presented by de Faria (2001). The load ratios may vary reflecting uncertainty in the applied mechanical loadings. By fixing load rations a nondimensional loading parameter $\lambda_0$ specifies the magnitude such that $\mathbf{N}_0$ is expressed as

$$\mathbf{N}_0 = -\lambda_0 \sum_{i=1}^{n} \mathbf{N}_{0i} R_i, \quad (11)$$

where $n$ is the number of loading cases and $\mathbf{N}_{0i}$ is the buckling load associated with loading $i$ when it is applied individually, i.e., when $R_i = 1.0$, $R_1 = R_2 = ... = R_{i-1} = R_{i+1} = ... = R_n = 0$ and $\phi_N = \phi_M = 0$ (no piezoelectric charges).

A network with many pairs of active patches may be placed over the host plate. Two voltages are associated to pair $j$: $\phi_{Nj}$ and $\phi_{Mj}$. In order to computed the piezoelectric residual stresses the number of membrane problems to be solved is equal to the number of pairs of patches. Making $\phi_{Nj} = 1$ V and $\phi_{Mj} = 0$ V, all the other patches maintained at 0 V, results in residual stresses $\mathbf{N}_{pj}^R$ can be computed. Given the linearity of the membrane piezoelectric problem, if a general voltage $\phi_{Nj}$ is applied, then it will result in residual stresses $\phi_{Nj}\mathbf{N}_{pj}^R$. Assuming $m$

pairs of patches simultaneously energized, the total residual stresses will be

$$\mathbf{N}_p^R = \sum_{j=1}^{m} \phi_{Nj} \mathbf{N}_{pj}^R. \tag{12}$$

Discretization of Eq. (10b) can now be conducted. Table 1 presents the continuous terms of Eq. (10b) and their discretized counterparts.

| Continuous | Discrete |
|---|---|
| $\int (\boldsymbol{\kappa}^T \mathbf{D} \boldsymbol{\kappa} + \boldsymbol{\gamma}^T \mathbf{A}_S \boldsymbol{\gamma}) d\Omega$ | $\mathbf{q}^T \mathbf{K} \mathbf{q}$ |
| $\int \boldsymbol{\epsilon}_N^T \mathbf{N}_0 d\Omega$ | $\mathbf{q}^T \mathbf{K}_G \mathbf{q}$ |
| $\int (\boldsymbol{\epsilon}^*)^T \mathbf{N}_0 d\Omega$ | $\mathbf{q}^T \mathbf{K}_G \mathbf{q}^*$ |
| $\int \boldsymbol{\epsilon}_N^T \mathbf{N}_p^R d\Omega$ | $\mathbf{q}^T \overline{\mathbf{K}}_G \mathbf{q}$ |
| $\int (\boldsymbol{\epsilon}^*)^T \mathbf{N}_p^R d\Omega$ | $\mathbf{q}^T \overline{\mathbf{K}}_G \mathbf{q}^*$ |
| $\int \boldsymbol{\kappa}^T \mathbf{M}_p d\Omega$ | $\mathbf{q}^T \mathbf{f}_{Mj}$ |

Table 1: Continuous vs. discretized terms

Matrix $\mathbf{K}$ is the stiffness matrix that also includes stiffness contributions from the piezoelectric patches. Vector $\mathbf{q}$ is the displacement vector. Vector $\mathbf{q}^*$ is the vector of initial imperfections. Matrix $\mathbf{K}_G$ is the traditional geometric stiffness matrix. Matrix $\overline{\mathbf{K}}_G$ is the geometric stiffness matrix associated with piezoelectric residual stresses. Notice that matrices $\mathbf{K}_G$ and $\overline{\mathbf{K}}_G$ are in fact associated with mechanical loading $i$ and voltage $j$ respectively such that the complete bending problem can be written as

$$\left( \mathbf{K} + \sum_{j=1}^{m} \phi_{Nj} \overline{\mathbf{K}}_{Gj} - \lambda_0 \sum_{i=1}^{n} R_i \mathbf{K}_{Gi} \right) \mathbf{q} =$$
$$- \left( \sum_{j=1}^{m} \phi_{Nj} \overline{\mathbf{K}}_{Gj} \right) \mathbf{q}^* + \lambda_0 \left( \sum_{i=1}^{n} R_i \mathbf{K}_{Gi} \right) \mathbf{q}^* + \sum_{j=1}^{m} \phi_{Mj} \mathbf{f}_{Mj}. \tag{13}$$

## 4 BUCKLING OPTIMIZATION AND PREBUCKLING ENHANCEMENT

The displacements of the plate are given by $\mathbf{q}$. Equation (13) shows that even small $\lambda_0$ induces displacements $\mathbf{q}$. The prebuckling enhancement consists in making $\mathbf{q}$ as small as possible, preferably identically zero, through application of the proper voltages $\phi_{Mj}$. However, this is usually unfeasible in practical application since the number of displacement degrees of freedom contained in $\mathbf{q}$ is usually far greater than $m$, the number of pairs of piezoelectric patches attached to the plate. Moreover, matrix $\mathbf{K} + \sum_{j=1}^{m} \phi_{Nj} \overline{\mathbf{K}}_{Gj} - \lambda_0 \sum_{i=1}^{n} R_i \mathbf{K}_{Gi}$ is almost singular in the imminence of buckling, meaning that $\mathbf{q}$ grows without bounds.

Given the practical constraints on forcing $\mathbf{q} = \mathbf{0}$ two other strategies are proposed to enhance prebuckling. First, the buckling load can be maximized if $\phi_{Nj}$ are carefully selected such that matrix $\mathbf{K} + \sum_{j=1}^{m} \phi_{Nj} \overline{\mathbf{K}}_{Gj} - \lambda_0 \sum_{i=1}^{n} R_i \mathbf{K}_{Gi}$ yields larger $\lambda_0$. Second, select $\phi_{Mj}$ to minimize somehow the right hand side of Eq. (13). Each strategy will be explored in the following.

### 4.1 Buckling load maximization

The traditional buckling eigenproblem can be extracted from Eq. (13):

$$\left(\mathbf{K}+\sum_{j=1}^{m}\phi_{Nj}\overline{\mathbf{K}}_{Gj}-\lambda\sum_{i=1}^{n}R_i\mathbf{K}_{Gi}\right)\mathbf{q}=\mathbf{0}, \tag{14}$$

where now $\lambda$ is the buckling load and $\mathbf{q}$ is the buckling mode. When the load ratios $R_i$ are maintained fixed the maximum $\lambda$ can be found by changing $\phi_{Nj}$. Usual optimization techniques may be used to obtain the optimal values of $\phi_{Nj}$. Nonetheless, a much more efficient optimization method can be employed stemming from the fact that the first buckling load $\lambda_1$ must be concave with respect to $\phi_{Nj}$ as will be proven.

If one fixes $R_i$'s then it is possible to define $\mathbf{K}_G=\sum_{i=1}^{n}R_i\mathbf{K}_{Gi}$. Additionally, if the $\phi_{Nj}$'s are also fixed the eigenproblem in Eq. (14) can be solved for the critical buckling load$\lambda_1$. Varying $\phi_{Nj}$'s new values for $\lambda_1$ are obtained. Thus, continously varying $\phi_{Nj}$'s the stability surface depicted in Fig. 2a for the most general situation is generated. Figure 2b illustrates the one-dimensional case. Vector $\mathbf{n}$, normal to the stability surface at point $C$, can be seen in Fig. 2 as well as hyperplane $\beta$ tangent to the stability surface.

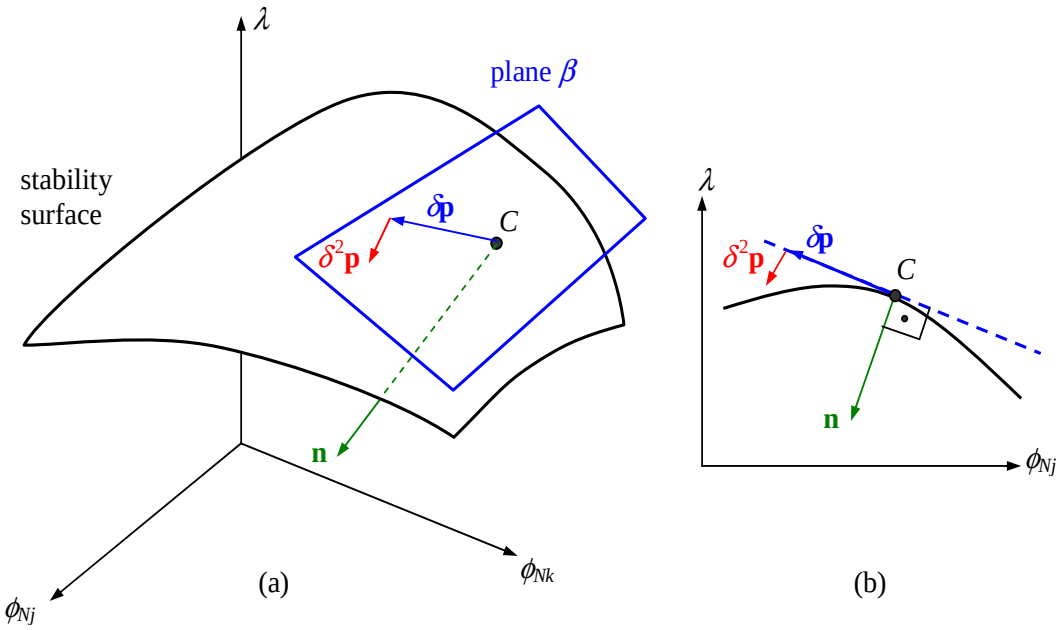


Figure 2: Stability surface

A point infinitesimally close to point $C$ can be obtained through perturbation of $\phi_{Nj}$ into $\phi_{Nj}+\delta\phi_{Nj}+\delta^2\phi_{Nj}+...$, which, in turn, result in perturbations in $\lambda_1$ of the form $\lambda_1+\delta\lambda_1+\delta^2\lambda_1+...$ and in $\mathbf{q}$ of the form $\mathbf{q}+\delta\mathbf{q}+\delta^2\mathbf{q}+....$ When perturbations in $\phi_{Nj}$, $\lambda_1$ and $\mathbf{q}$ are introduced in Eq. (14) it becomes

$$\left[\mathbf{K}+\sum_{j=1}^{m}(\phi_{Nj}+\delta\phi_{Nj}+\delta^2\phi_{Nj}+...)\overline{\mathbf{K}}_{Gj}-(\lambda_1+\delta\lambda_1+\delta^2\lambda_1+...)\mathbf{K}_G\right]\times$$

$$(\mathbf{q}+\delta\mathbf{q}+\delta^2\mathbf{q}+...)=\mathbf{0}. \tag{15}$$

The zero, first and second order eigenproblems are given by

$$\left(\mathbf{K}+\sum_{j=1}^{m}\phi_{Nj}\overline{\mathbf{K}}_{Gj}-\lambda_1\mathbf{K}_G\right)\mathbf{q}=\mathbf{0},$$

$$\left(\sum_{j=1}^{m}\delta\phi_{Nj}\overline{\mathbf{K}}_{Gj}-\delta\lambda_1\mathbf{K}_G\right)\mathbf{q}+\left(\mathbf{K}+\sum_{j=1}^{m}\phi_{Nj}\overline{\mathbf{K}}_{Gj}-\lambda_1\mathbf{K}_G\right)\delta\mathbf{q}=\mathbf{0},$$

$$\left(\sum_{j=1}^{m}\delta^2\phi_{Nj}\overline{\mathbf{K}}_{Gj}-\delta^2\lambda_1\mathbf{K}_G\right)\mathbf{q}+\left(\sum_{j=1}^{m}\delta\phi_{Nj}\overline{\mathbf{K}}_{Gj}-\delta\lambda_1\mathbf{K}_G\right)\delta\mathbf{q}+$$

$$\left(\mathbf{K}+\sum_{j=1}^{m}\phi_{Nj}\overline{\mathbf{K}}_{Gj}-\lambda_1\mathbf{K}_G\right)\delta^2\mathbf{q}=\mathbf{0}. \tag{16}$$

The multiplication of Eq. (16a) by $\mathbf{q}^T$ from the left yields the equation of the hyperplane $\beta$ defined in the $\phi_{N1}\phi_{N2}...\phi_{Nm}\lambda$ space and given by Eq. (17) below

$$\mathbf{q}^T\mathbf{K}\mathbf{q}+\sum_{j=1}^{m}\phi_{Nj}(\mathbf{q}^T\overline{\mathbf{K}}_{Gj}\mathbf{q})-\lambda_1(\mathbf{q}^T\mathbf{K}_G\mathbf{q})=0. \tag{17}$$

while the multiplication of Eq. (16b) by $\mathbf{q}^T$ from the left and using Eq. (16a) leads to

$$\delta\mathbf{p}^T\mathbf{n}=0, \tag{18}$$

where

$$\delta\mathbf{p}=\{\ \delta\phi_{N1}\quad\delta\phi_{N2}\quad ...\quad\delta\phi_{Nm}\quad\delta\lambda_1\ \}^T,$$
$$\delta^2\mathbf{p}=\{\ \delta^2\phi_{N1}\quad\delta^2\phi_{N2}\quad ...\quad\delta^2\phi_{Nm}\quad\delta^2\lambda_1\ \}^T,$$

$$\mathbf{n}=\{\ \mathbf{q}^T\overline{\mathbf{K}}_{G1}\mathbf{q}\quad\mathbf{q}^T\overline{\mathbf{K}}_{G2}\mathbf{q}\quad ...\quad\mathbf{q}^T\overline{\mathbf{K}}_{Gm}\mathbf{q}\quad-\mathbf{q}^T\mathbf{K}_G\mathbf{q}\ \}^T. \tag{19}$$

Geometrically, Eq. (18) proves that vector **n** is normal to the stability surface. Thus, plane $\beta$ is tangent to the stability surface since **n** is normal to $\beta$ according to Eq. (17). Notice that the $\lambda$ component of **n** has a negative sign. When the first critical buckling load is positive $\mathbf{q}^T\mathbf{K}_G\mathbf{q}$ is positive. Thus, the $\lambda$ component of **n**, $-\mathbf{q}^T\mathbf{K}_G\mathbf{q}$, is negative as illustrated in Fig. 2. In the case when the first critical buckling load is negative, $\mathbf{q}^T\mathbf{K}_G\mathbf{q}$ must also be negative and $-\mathbf{q}^T\mathbf{K}_G\mathbf{q}$ is positive.

Multiplication of Eq. (16c) by $\mathbf{q}^T$ from the left and using Eq. (16a) leads to

$$\mathbf{q}^T\left(\sum_{j=1}^{m}\delta^2\phi_{Nj}\overline{\mathbf{K}}_{Gj}-\delta^2\lambda_1\mathbf{K}_G\right)\mathbf{q}+\mathbf{q}^T\left(\sum_{j=1}^{m}\delta\phi_{Nj}\overline{\mathbf{K}}_{Gj}-\delta\lambda_1\mathbf{K}_G\right)\delta\mathbf{q}=\mathbf{0}. \tag{20}$$

and by multiplying Eq. (16b) by $\delta\mathbf{q}^T$ from the left and recalling that all matrices involved are symmetric leads to

$$\mathbf{q}^T\left(\sum_{j=1}^{m}\delta\phi_{Nj}\overline{\mathbf{K}}_{Gj}-\delta\lambda_1\mathbf{K}_G\right)\delta\mathbf{q}=-\delta\mathbf{q}^T\left(\mathbf{K}+\sum_{j=1}^{m}\phi_{Nj}\overline{\mathbf{K}}_{Gj}-\lambda_1\mathbf{K}_G\right)\delta\mathbf{q}. \tag{21}$$

The substitution of Eq. (21) into Eq. (20) yields

$$-\delta^2\lambda_1(\mathbf{q}^T\mathbf{K}_G\mathbf{q}) + \sum_{j=1}^{m}\delta^2\phi_{Nj}(\mathbf{q}^T\overline{\mathbf{K}}_{Gj}\mathbf{q}) - \delta\mathbf{q}^T\left(\mathbf{K} + \sum_{j=1}^{m}\phi_{Nj}\overline{\mathbf{K}}_{Gj} - \lambda_1\mathbf{K}_G\right)\delta\mathbf{q} = 0. \quad (22)$$

while the substitution of Eqs. (19b) and (19c) into Eq. (22) leads to

$$\delta^2\mathbf{p}^T\mathbf{n} = \delta\mathbf{q}^T\left(\mathbf{K} + \sum_{j=1}^{m}\phi_{Nj}\overline{\mathbf{K}}_{Gj} - \lambda_1\mathbf{K}_G\right)\delta\mathbf{q} \geq 0, \quad (23)$$

where the inequality sign holds since $\mathbf{K} + \sum_{j=1}^{m}\phi_{Nj}\overline{\mathbf{K}}_{Gj} - \lambda_1\mathbf{K}_G$ is positive semi-definite. Equation (23) shows that the second order tangent vector to the stability surface $\delta^2\mathbf{p}$ and the normal vector $\mathbf{n}$ are oriented in the same direction. This can be visualized in Fig. 2. Therefore, from the differential geometry argument presented, it is concluded that the stability surface is concave with respect to the origin of the $\phi_{N1}\phi_{N2}...\phi_{Nm}\lambda$ space. The concavity of the stability surface is of utmost importance when it comes to buckling load maximization.

The maximum $\lambda_1$ is sought through the variation of the involved $\phi_{Nj}$'s. However, due to physical limitations, the values of $\phi_{Nj}$ are bounded by the breakdown voltage such that $\phi_{\min,j} \leq \phi_{Nj} \leq \phi_{\max,j}$. The concavity of the stability surface implies that there are only three possibilities for its orientation as shown in Figs. 3a-3c. Either $\partial\lambda_1/\partial\phi_{Nj}(\phi_{\min,j})$ and $\partial\lambda_1/\partial\phi_{Nj}(\phi_{\max,j})$ have the same sign (Figs. 3a and 3b) or they have opposite signs (Fig. 3c). Notice that these derivatives can be readily computed by

$$\frac{\partial\lambda_1}{\partial\phi_{Nj}} = \frac{\mathbf{q}^T\overline{\mathbf{K}}_{Gj}\mathbf{q}}{\mathbf{q}^T\mathbf{K}_G\mathbf{q}}. \quad (24)$$

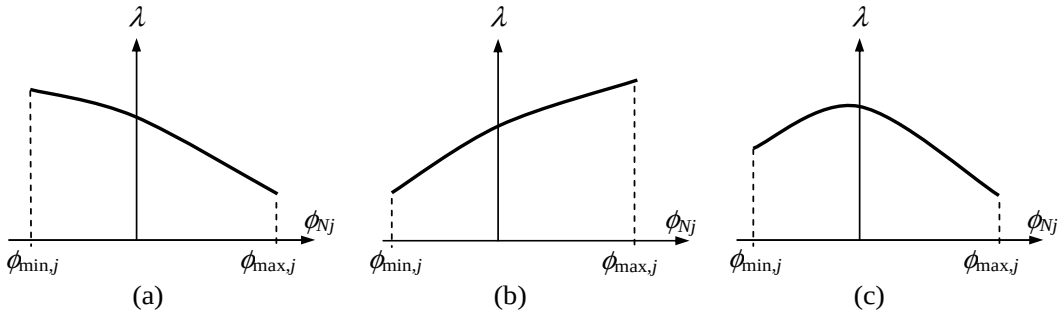


Figure 3: Stability surface orientation

In the first two cases the maximum $\lambda_1$ must be associated with one of the vertices of the envelope defined by the inequalities $\phi_{\min,j} \leq \phi_{Nj} \leq \phi_{\max,j}$ where $j = 1, 2, ..., m$. For a three-dimensional case this envelope is shown in Fig. 4. Observe that in general $\phi_{\min,j} \neq \phi_{\min,k}$ and $\phi_{\max,j} \neq \phi_{\max,k}$. Points $V_1, ..., V_8$, are those that must be checked and the maximum $\lambda_1$ associated with these eight points is the solution to the critical buckling load maximization problem. On the other hand, if stability surface orientation is such as depicted in Fig. 3c then a conventional optimization method must be used to obtain the maximum $\lambda_1$. However, given the concavity of the stability surface, its convergence is certainly very quick.

The preceding analysis assumed that the load ratios $R_i$ are maintained fixed. However, in real situations, a structure may be subject to several load cases during its operation and, therefore,

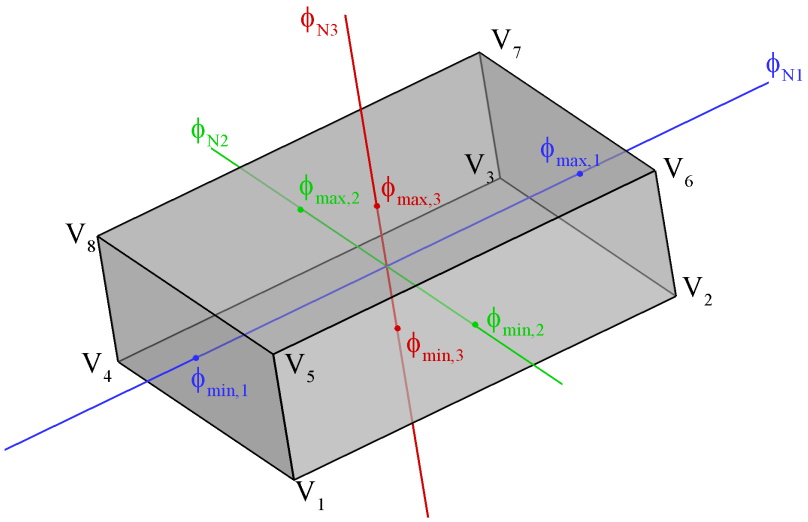


Figure 4: Voltage envelope

there is variation or uncertainty associated with the load ratios. In de Faria (2001) a technique is proposed to handle the lack of specification in $R_i$ that can be employed in the present investigation. A reformulation of the optimization problem at hand is given in Eq. (25)

$$\max_{\phi_{Nj}} \min_{R_i} \lambda_1(\phi_{Nj}, R_i). \tag{25}$$

Firstly, the worst $\lambda_1$ is obtained for all possible ranges of $R_i$. Secondly, the technique just described is used to obtain the best $\phi_{Nj}$.

### 4.2 Mitigation of initial imperfections

The procedure presented in the preceding subsection is able to provide the best $\lambda_1$. However, the deleterious effects of initial imperfections has not yet been addressed. The left-hand side of Eq. (13) can be optimized for maximum $\lambda_1$. If the right-hand side of Eq. (13) is made identically zero then the resulting displacement field $\mathbf{q}$ is zero. Nevertheless, zeroing the right-hand side is not feasible in practice because the number of degrees of freedom present in $\mathbf{q}$ exceeds the number of voltages $\phi_{Mj}$ that can be appropriately selected.

The voltages $\phi_{Nj}$ are assumed to have been selected by the optimization procedure described previously, i.e., the optimization problem posed in Eq. (25) has been solved, to obtain the optimal solution $\phi_{Nj}$ and $R_i$. Hence, voltages $\phi_{Mj}$ are the only available degrees of freedom for use in ameliorating the effects of the imperfections.

A better understanding of the behavior of the force term present in the right-hand side of Eq. (13) is gained if $\mathbf{q}$ is spanned in the eigenvectors basis. Given that the buckling eigenproblem has been already resolved, it is plausible to assume that the corresponding eigenpairs $\lambda_k$, $\mathbf{q}_k$, $k = 1, 2, ..., n_\lambda$ are available, where $n_\lambda$ is the problem dimension or the total number of displacement degrees of freedom. Hence

$$\mathbf{q} = \sum_{k=1}^{n_\lambda} a_k \mathbf{q}_k, \tag{26}$$

where $a_k$ are coefficients to be determined. Substitution of Eq. (26) into (13) and multiplication

by $\mathbf{q}_k^T$ from the left leads to

$$a_k = \frac{1}{(\mathbf{q}_k^T \mathbf{K}_G \mathbf{q}_k)(\lambda_k - \lambda_0)} \mathbf{q}_k^T \left[ - \left( \sum_{j=1}^{m} \phi_{Nj} \overline{\mathbf{K}}_{Gj} \right) \mathbf{q}^* + \lambda_0 \left( \sum_{i=1}^{n} R_i \mathbf{K}_{Gi} \right) \mathbf{q}^* + \sum_{j=1}^{m} \phi_{Mj} \mathbf{f}_{Mj} \right], \tag{27}$$

where $\mathbf{K}_G = \sum_{i=1}^{n} R_i \mathbf{K}_{Gi}$.

Eq. (27) is the germane for the geometric imperfection mitigation procedure. The term $(\lambda_k - \lambda_0)$ in the denominator causes unbounded growth of $a_k$ as $\lambda_0 \rightarrow \lambda_k$. Therefore, the most critical of all $a_k$ is precisely $a_1$, which relates to the first buckling mode, since $\lambda_0$ reaches $\lambda_1$ first as it increases. Given that the entire right-hand side of Eq. (13) cannot be made zero simultaneously, the second best procedure is to make it orthogonal to $\mathbf{q}_1$, i.e., to force the numerator in Eq. (27) equal to zero. This condition yields one linear algebraic equation in $\phi_{Mj}$'s. Thus, if there are $m$ pairs of actuators, in principle it is possible to enforce $a_1 = a_2 = ... = a_m = 0$ resulting in $m$ linear algebraic equations to be solved. In practice this process is not so straightforward because there are restrictions imposed on $\phi_{Mj}$ by the breakdown voltages. These restrictions can be relaxed if the actuators are wisely positioned over the host plate.

There are two sources of uncertainty in the proposed procedure. It was assumed that the load ratios $R_i$'s are known from the maximization of the critical buckling load $\lambda_1$, but it is possible they vary. Since voltages $\phi_{Mj}$ were selected based on the worst $R_i$'s, the variation of the load ratios destroys the orthogonality condition imposed between $\mathbf{q}_k^T$ and the right-hand side of Eq. (13). Even if the orthogonality is destroyed, the robust optimization procedure proposed in Eq. (25) guarantees that $\lambda_1$ increases when the $R_i$'s vary which, again, works in favor of mitigation of the imperfection effects.

## 5 NUMERICAL RESULTS

The physical properties and geometric parameters given in Tab. 2 will be used in the numerical simulations. The plate is 40 cm $\times$ 30 cm with the larger side along the $x$ axis. One pair of 4 cm $\times$ 3 cm piezoelectric actuators is used. It is located at the center of the plate and aligned with the plates edges as shown in Fig. 1. Two laminates are considered: cross-ply laminate $[0/90]_S$ and $[\pm 45]_S$ with four layers of 0.15 mm thickness each. The thickness of the piezoelectric actuators (top and bottom) is 0.05 mm. A depoling field of 1000 V/mm is assumed.

| Property | G1195N | T300/5208 |
|---|---|---|
| Young modulus $E_{11}$ (GPa) | 63.0 | 154.5 |
| Young modulus $E_{22}$ (GPa) | 63.0 | 11.13 |
| Poisson ratio $\nu_{12}$ | 0.3 | 0.304 |
| Shear modulus $G_{12} = G_{13}$ (GPa) | 24.2 | 6.98 |
| Shear modulus $G_{23}$ (GPa) | 24.2 | 3.36 |
| Piezoelectric constant $e_{31}$ (N/V m) | 17.6 | - |
| Piezoelectric constant $e_{32}$ (N/V m) | 17.6 | - |
| Depoling field $E_{\text{MAX}}$ (V/mm) | 1000 | - |

Table 2: Physical properties

Boundary conditions are imposed for three problems as follows. Firstly, the piezoelectric

problem given by Eq. (10a) is solved with $N_{xx0} = N_{yy0} = N_{xy0} = 0$ with the boundary conditions being $u = v = 0$ along the four edges of the plates. The piezoelectric patch contracts the plate when energized with a negative $\phi_N$. The edges will react by creating traction residual forces $\mathbf{N}_p^R$ that stiffen the plate. On the other hand, a positive $\phi_N$ induces compressive $\mathbf{N}_p^R$, an undesirable development since it softens the plate. Secondly, the mechanical problem given by Eq. (10a) is solved with $\mathbf{N}_0 \neq \mathbf{0}$ and $\mathbf{N}_p = \mathbf{0}$ with boundary conditions imposed on only $u$ and $v$. Thirdly, the bending problem given by Eq. (10b) is solved by imposing simply supported conditions on $w$, $\psi_x$ and $\psi_y$ along the four edges.

The mesh used has 20 $\times$ 20 biquadratic elements. The piezoelectric actuators are modeled with four elements as shown in Fig. 5.

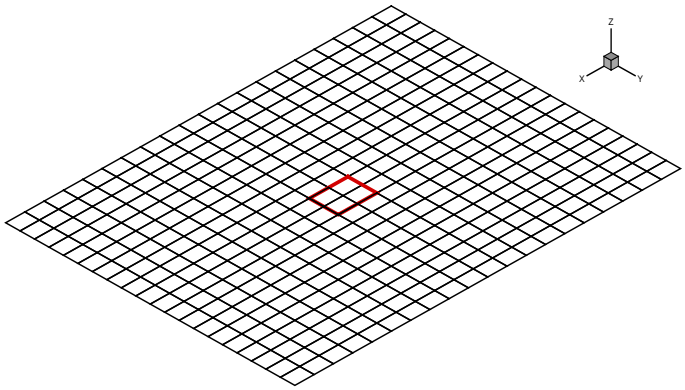


Figure 5: Mesh

The first measure to enhance prebuckling behavior is to increase the buckling load by proper choice of $\phi_N$ against the load ratios $R_i$. Three types of traditional loadings are applied: (i) uniform compressive loading along the $x$ direction ($\lambda_{xx}$) (ii) uniform compressive loading along the $y$ direction ($\lambda_{yy}$) and (iii) uniform shear ($\lambda_{xy}$). The actuator voltage is varied within the limits of the depoling field, i.e., -50 V $\leq \phi_N \leq$ +50 V. Fig. 6 presents the curves obtained for the $[0/90]_S$ and $[\pm 45]_S$ laminates. The $\lambda_{yy}$ curve overlays the $\lambda_{xx}$ curve. $\lambda$ varies almost linearly with $\phi_N$ but a small concavity can be observed in $\lambda_{xy}$. These curves have been normalized for the case when $\phi_N$ = 0 V leading to buckling loads of 329.4 N/m ($x$ direction), 185.3 N/m ($y$ direction), 598.5 N/m (shear) for the $[0/90]_S$ laminate and 549.7 N/m ($x$ direction), 312.9 N/m ($y$ direction), 1685.9 N/m (shear) for the $[\pm 45]_S$ laminate. Buckling occurs under no mechanical loading for some value of $\phi_N >$ +50 V for all types of loading. This conclusion is intuitive; compressive residual stresses arise when positive voltages are applied impairing buckling behavior. The maximum $\lambda_{xx}$, $\lambda_{yy}$ and $\lambda_{xy}$ are associated with $\phi_N$ = -50 V. It can be observed that the $[\pm 45]_S$ laminate is less sensitive to variations in $\phi_N$. This is evidence that sensitivity to $\phi_N$ is associated with the laminate lay-up. The $[\pm 45]_S$ laminate will suffer from buckling due to residual stresses only for a value of $\phi_N$ substantially above +50 V.

From Fig. 6 it is clear that a situation like that shown in Fig. 3a is encountered and the best strategy is simply to select $\phi_N$ = -50 V. However, this voltage corresponds to the breakdown voltage of the piezoelectric film meaning that no $\phi_M$ can be applied without destroying the polarization of the piezoceramic. If geometric imperfections exist then it may be desirable to apply some $\phi_M \neq 0$ V. In order to investigate this possibility a cubic pattern of geometric

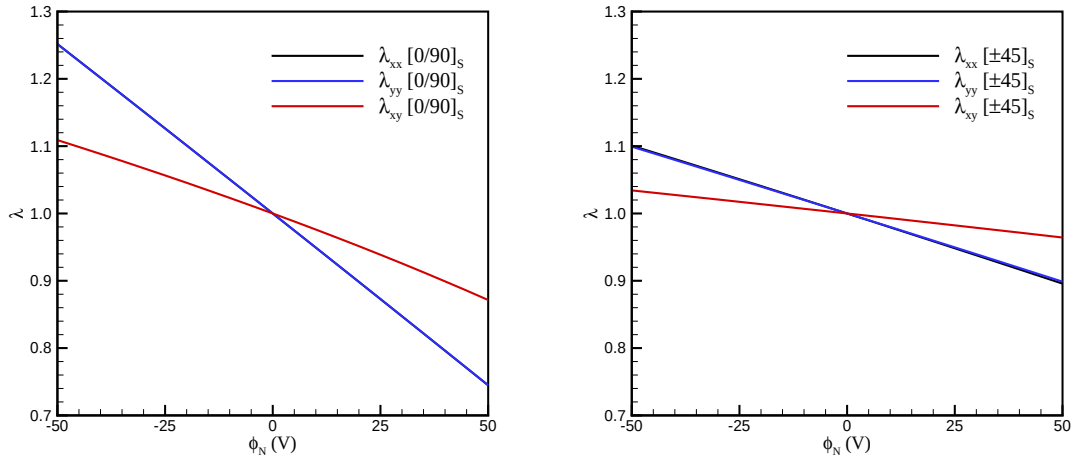


Figure 6: The variation of buckling load with voltage for different laminates

imperfections is adopted as:

$$w^*(x,y) = 16\mu h \frac{x}{a}\left(1-\frac{x}{a}\right)\left[1+\beta_x\left(1-\frac{2x}{a}\right)\right]\frac{y}{b}\left(1-\frac{y}{b}\right)\left[1+\beta_y\left(1-\frac{2y}{b}\right)\right], \quad (28)$$

where $a$ and $b$ are the plate side lengths ($a$ = 40 cm, $b$ = 30 cm), $\mu$ is a nondimensional parameter that controls the amplitude and $\beta_x$, $\beta_y$ are nondimensional parameters that control the degree of anti-symmetry in the pattern. Notice that symmetry is implied with respect to the plate center. Since four layers of 0.15 mm are used, $h$ = 0.6 mm in Eq. (28). According to this pattern $w^*(a/2, b/2) = \mu h > 0$. Hence, negative $\phi_M$ should be applied to attenuate the imperfections. In the simulations that follow $\mu = 0.5$.

The corresponding results for the case when the degree of anti-symmetry, as given by parameters $\beta_x$ and $\beta_y$, is null, are depicted in Figs. 7 and 8 for the $[0/90]_S$ and the $[\pm 45]_S$ laminates, respectively. These curves display the maximum absolute value of the transverse displacement $|w|$ over the plate as a function of the loading parameter $\lambda_0$. Figs. 7a and 8a refer to $\lambda_{xx}$ loading, Figs. 7b and 8b refer to $\lambda_{yy}$ loading, and Figs. 7c and 8c refer to $\lambda_{xy}$ loading.

The plots presented in all cases can be compared to the scenario where there is no actuation, i.e., when $\phi_N = \phi_M$ = 0 V. In this no actuation case $w_{\mathrm{MAX}}$ rapidly grows as $\lambda_0$ increases. Notice that when $\lambda_0 = 0$ generally $w_{\mathrm{MAX}} \neq 0$. This is explained by Eq. (13) whose right-hand side contains two terms that are nonzero even when $\lambda_0 = 0$. In all situations making $\phi_N$ = -50 V is highly effective although in some cases a blend with $\phi_M \neq 0$ proves to be more efficient such as in Figs. 7c and 8c for higher values of $\lambda_0$. A degree of anti-symmetry is introduced by making $\beta_x = \beta_y = 5$ in Eq. (28). Now Figs. 9 and 10 are plotted for the $[0/90]_S$ and $[\pm 45]_S$ laminates respectively.

The most striking observation is that when anti-symmetry is present in the imperfections pattern the strategy of applying $\phi_M$ is not as effective. On the contrary, Figs. 8c and 10c show that making $\phi_N$ = 0 V and $\phi_M$ = -50 V impairs the prebuckling response. It seems therefore that the best action is to make $\phi_N$ as high as possible while maintaining $\phi_M$ = 0 V. This, however, is a hasty conclusion. Note that only one actuator is affixed to the center of the plate. This particular location is best suited for symmetric imperfection patterns. If anti-symmetric patterns exist then it would be more efficient to have a network of actuators. This

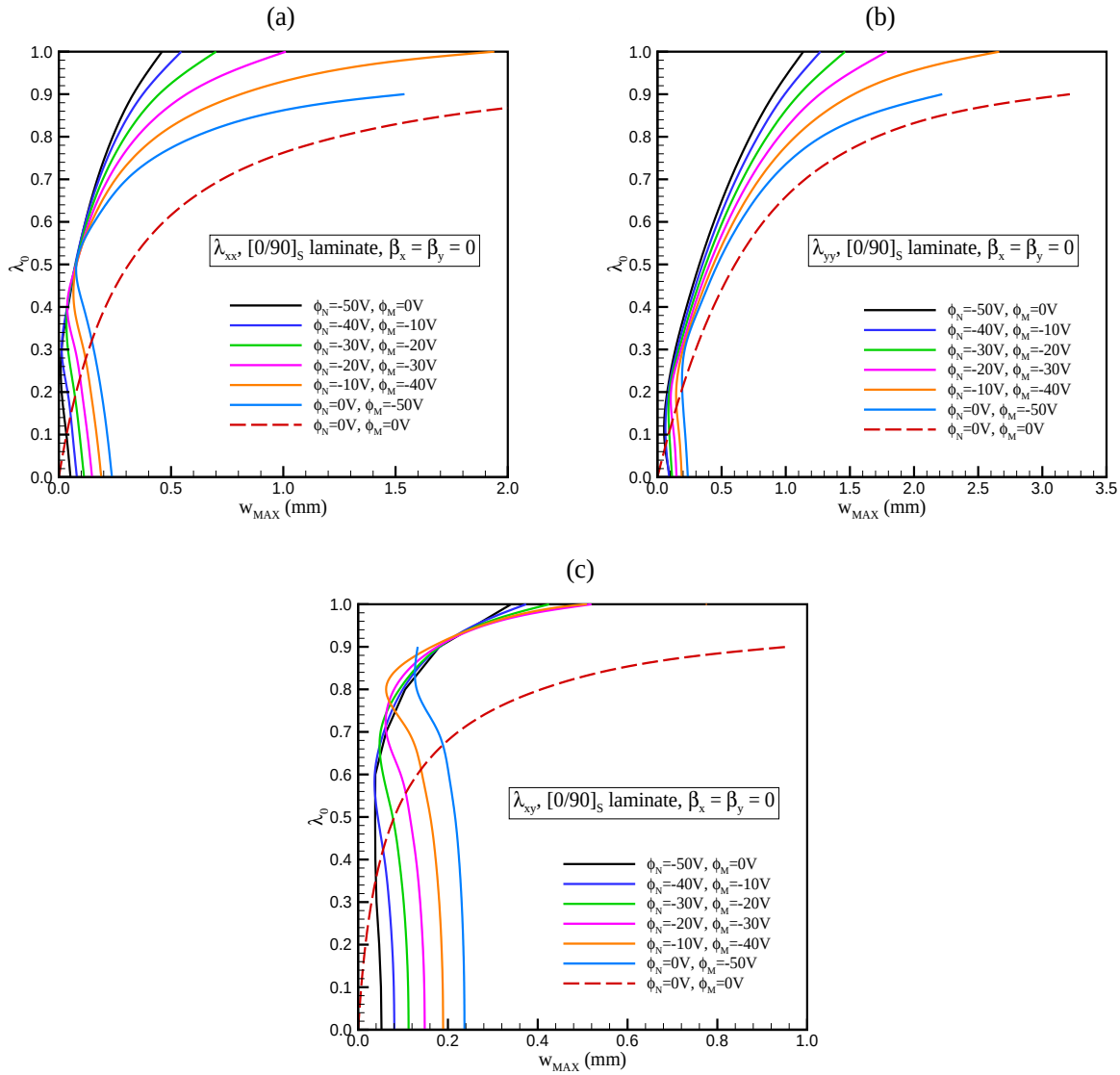


Figure 7: $[0/90]_S$ laminated plate, $\beta_x = \beta_y = 0$

is possess the interesting problem: how can the locations of piezoelectric patches be optimally selected to enhance prebuckling and remain insensitive to arbitrary imperfection patterns?

## 6 CONCLUSIONS

Two techniques have been proposed: one to maximize buckling loads of smart composite plates through piezoelectric residual stress stiffening effects and another to enhance the prebuckling response when initial geometric imperfections are present by eliminating contributions of the first buckling modes. Moreover, it is shown that the best results are obtained when both strategies are employed in combination.

For the sake of demonstration only one pair of active patches has been used. In real applications a network of patches can be used. This would certainly be better since more patches allow one to induce residual stresses in regions where they are most effective and it would also allow more freedom to alleviate the effects of a number of imperfection patterns. This is a practical concern since imperfections may be randomly distributed meaning that each particular plate

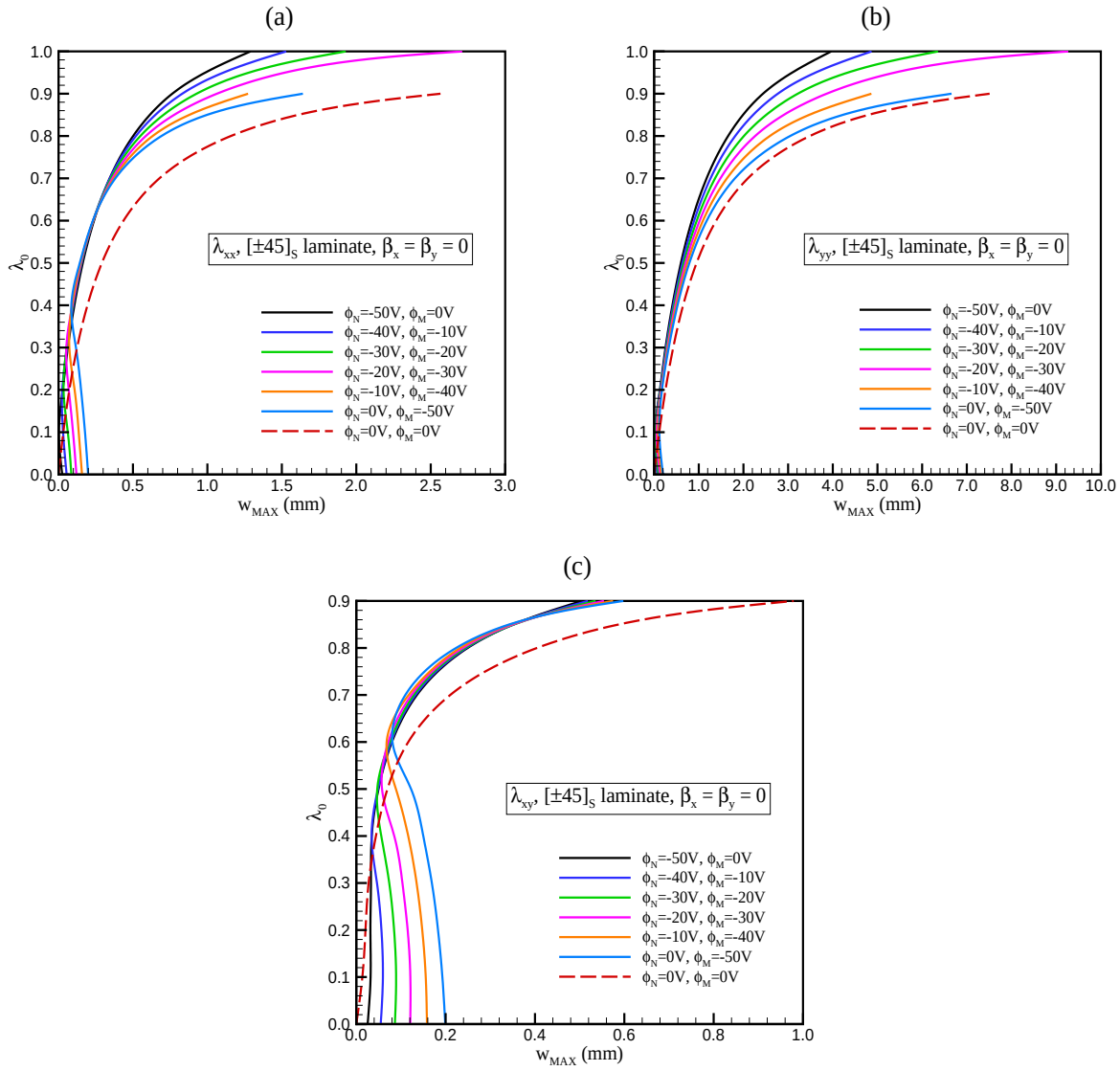


Figure 8: $[\pm45]_S$ laminated plate, $\beta_x = \beta_y = 0$

fabricated has its own optimal location of active patches.

$\phi_M$ has been held constant throughout the simulations. However, the best procedure is certainly to increase $\phi_M$ as $\lambda_0$ increases. This conclusion is obvious from Figs. 7-10. One simple strategy would be to make $\phi_M$ proportional to $\lambda_0$. However, the most effective is to use sensors that are able to detect the plate response and to have a control system commanding the actuators according to the sensors data.

Uncoupling the membrane and bending problems is a key to the success of the techniques proposed. In general imperfect smart shells the situation is more complex since the uncoupling cannot be done. In this case the full nonlinear problem must be solved considering simultaneously all degrees of freedom (membrane and bending). The proper nonlinear numerical methods, such as Newton-Raphson, must then be called upon.

## 7 ACKNOWLEDGEMENTS

This work was partially financed by the Brazilian agency CNPq (grant no. 300236/2009-3).

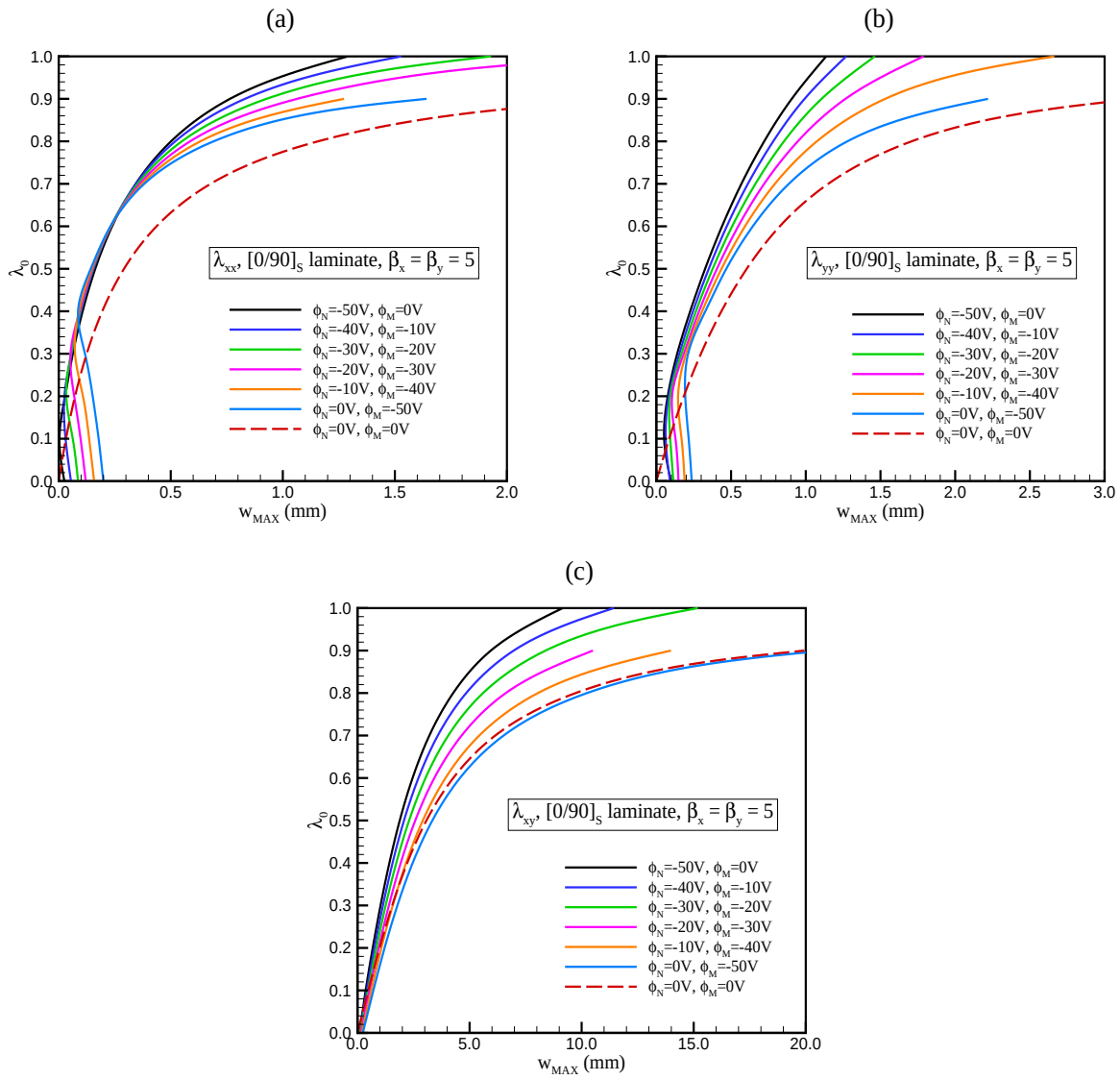


Figure 9: $[0/90]_S$ laminated plate, $\beta_x = \beta_y = 5$

## REFERENCES

[1] Crawley, E.F. and de Luis, J. Use of piezoelectric actuators as elements of intelligent structures, *AIAA Journal*, 25(10), 1373-1385, 1987.

[2] Reddy, J.N. *Mechanics of laminated composite plates: theory and analysis*, CRC Press, Boca Raton, 1997.

[3] Varelis, D. and Saravanos, D.A. Coupled buckling and postbuckling analysis of active laminated piezoelectric composite plates, *International Journal of Solids and Structures*, 41(5-6), 1519-1538, 2004.

[4] Rabinovitch, O. Geometrically nonlinear behavior of piezoelectric laminated plates, *Smart Materials and Structures*, 14(4), 785-798, 2005.

[5] Chandrashenkhara, K. and Bathia, K. Active buckling control of smart composite plates - finite element analysis, *Smart Materials and Structures*, 2(1), 31-39, 1993.

[6] Meressi, T. and Paden, B. Buckling control of a flexible beam using piezoelectric actuators, *Journal of Guidance, Control and Dynamics*, 16(5), 977-980, 1993.

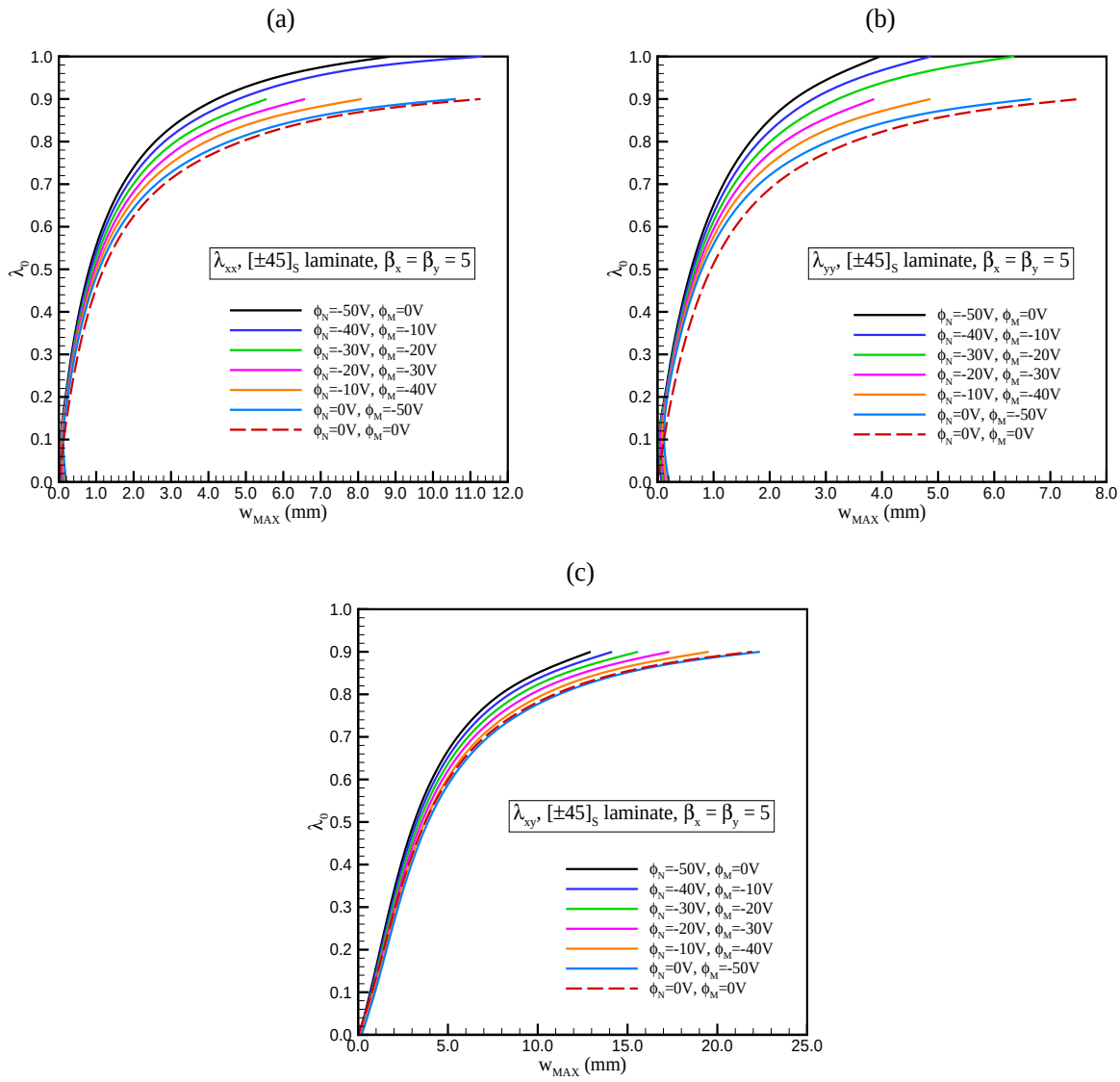


Figure 10: $[\pm 45]_S$ laminated plate, $\beta_x = \beta_y = 5$


[7] Correia, V.M.F. and Mota Soares, C.M. and Mota Soares, C.A. Buckling optimization of composite laminated adaptive structures, *Composite Structures*, 62(3), 315-321, 2003.

[8] Nye, N.Y. *Physical properties of crystals: their representation by tensors and matrices*, Oxford University Press, London, 1972.

[9] de Faria, A.R. and Hansen, J.S. On buckling optimization under uncertain loading combinations, *Structural and Multidisciplinary Optimization*, 21(4), 272-282, 2001.